# Synthesis, Characterization And Electrochemical Studies Of Mgfe<sub>2</sub>O<sub>4</sub> Qds For Efficient Electrochemical Supercapacitor Electrode

# R.M.Regma Infant<sup>1</sup>, S.R. Gibin<sup>2,3</sup>, Joselin Beaula T<sup>4,6</sup>, J.Samuel<sup>5</sup>

- <sup>1</sup>Research Scholar, Department of Physics and Research Centre, Malankara Catholic College, Mariagiri, Kaliakkavilai-629153, Tamil Nadu, India.
- <sup>2</sup>Formerly Assistant Professor, Department of Physics and Research Centre, Malankara Catholic College, Mariagiri - 629153, Tamil Nadu, India
- <sup>3</sup>Associate Professor of Physics, Sree Sakthi Engineering College (Autonomous), Karamadai, Coimbatore-641104, Tamil Nadu, India
- <sup>4</sup>Assistant Professor, Department of Physics and Research Centre, Malankara Catholic College, Mariagiri 629153, Tamil Nadu, India
- <sup>5</sup>Associate Professor of Physics, Cape Institute of Technology Levengipuram-627114, Tamil Nadu, India. <sup>6</sup>Manonmaniam Sundaranar University, Abishekapatti-627012, Tirunelveli, Tamil Nadu, India.

## Abstract

In this study, MgFe<sub>2</sub>O<sub>4</sub> quantum dots (QDs) were synthesized using a cost-effective co-precipitation method. The synthesized MgFe<sub>2</sub>O<sub>4</sub> QDs were thoroughly characterized through various methods, especially X-Ray Diffraction (XRD), Transmission Electron Microscopy (TEM), Scanning Electron Microscopy (SEM) with Energy-Dispersive X-ray Analysis (EDX), X-ray photoelectron spectroscopy (XPS), Fourier Transform Infrared spectroscopy (FTIR), and Thermogravimetric and Differential Thermal Analysis (TG/DTA). XRD and FTIR analyses proved the spinel structure of the synthesized material, while XPS scrutiny verified the being of Fe 2p, Mg 2p, and O 1s in the MgFe<sub>2</sub>O<sub>4</sub> QDs. Additionally, the electrochemical characteristics of the material were estimated using cyclic voltammetry (CV), revealing high electrochemical capacitance, outstanding rate performance, and stable cycling behaviour. These discovers indicate that MgFe<sub>2</sub>O<sub>4</sub> QDs serve as promising electrode materials, exhibiting high particular capacitance and good retention. Owing to their remarkable synergistic effects, MgFe<sub>2</sub>O<sub>4</sub> QDs hold significant potential for applications in various electrochemical fields.

Keywords: Quantum dots, Co-precipitation technique, Spinel structure, Impedance, Supercapacitor.

## 1. INTRODUCTION

Supercapacitors are extremely suitable for applications that require power flux density and fast charging, such as power emergency actuators in aviation, series hybrids, electronic flashes, energy carrier screwdrivers, enclosed ski lift, and other power electronic devices [1]. They also play a crucial role in stabilizing electronic power converters and potential difference in industries where load fluctuations pose a significant challenge [2]. Furthermore, pliable supercapacitors are widely utilized in wearable and portable electronics, capable of functioning under bending and twisting conditions.

Several studies have reported that ferrites exhibit excellent chemical and thermal stability at the nanoscale, displaying unique chemical and physical properties [3]. Recently, nano-sized magnesium ferrite particles have garnered attention due to their distinctive characteristics, making them suitable for various applications, including high-density data storage, high-frequency devices, and magnetic refrigeration [4]. Additionally, nanostructured magnetic materials have fascinated increasing interest due to their novel properties, which differ significantly from their bulk counterparts [5-7]. Specifically, ordered magnetic nanostructures such as nanorods and nanowires have been extensively studied for their enhanced electrical and thermal properties [8].

Quantum dots (QDs) play a critical role in technological and electronic applications. To optimize their use, it is essential to understand their unique physical and chemical properties in comparison to bulk materials [9-13]. Due to their small size and broad application potential, QDs have become one of the most generally studied facilitated across various current fields. Quantum dots with size of approximately 10 nm have attracted significant interest due to their small and symmetrical photoemission, tuneable emission, strong illumination, and excellent photostability [9-11]. In most applications, the properties of artificially engineered ultra-small nanostructures are largely influenced by their size and morphology, making QDs distinct from other synthesized structures [12].

ISSN: 2229-7359 Vol. 11 No. 18s, 2025

https://theaspd.com/index.php

Nanotechnology has significantly contributed to advancements in accumulator devices such as supercapacitors and batteries by enhancing their electrical and physiochemical properties. Spinel-phase nanoparticles hold great promise in energy storage applications, particularly as electrode materials for Liion batteries [14]. Metal ferrite nanoparticles have demonstrated excellent electrical conductivity, high specific capacity, enhanced electrochemical reactivity, and cost-effectiveness for energy production. Supercapacitors, in particular, have emerged as a hopeful energy storage solution, contributing notable benefits over traditional storage batteries and dielectric capacitors [15]. Their high-power density, superior integration with sustainable energy sources, extended lifespan, and stable performance make them an attractive alternative [16-18]].

During the last two decades, the co-precipitation method has gained notable attention for synthesizing metal oxides with precisely controlled compositions. This study focuses on the combination and electrical properties of MgFe<sub>2</sub>O<sub>4</sub> quantum dots (QDs) fabricated using the co-precipitation method for supercapacitor applications. The synthesized samples were analysed using X-ray diffraction (XRD) to determine their crystalline structure. Additionally, the sample was subjected to annealing at 700°C was further examined through scanning electron microscopy (SEM), high-resolution transmission electron microscopy (HR-TEM), cyclic voltammetry (CV), Braeuer-Emmett-Teller (BET) analysis, Fourier transform infrared spectroscopy (FTIR), and X-ray photoelectron spectroscopy (XPS). These characterization techniques provided comprehensive insights into the structural, morphological, electrochemical, surface area, and chemical properties of the magnesium ferrite nanoparticles.

## 2.Experimental

## 2.1Synthesis of MgFe<sub>2</sub>O<sub>4</sub> QDs

The precursor for  $MgFe_2O_4$  quantum dots (QDs) was synthesized using a novel chemical precipitation method, with  $MgFe_2O_4$  serving as the precipitant. All reagents used in the process were obtained from Merck Chemicals. Initially, magnesium nitrate ( $Mg(NO_3)_2 \cdot 4H_2O$ ), iron nitrate ( $Fe(NO_3)_2 \cdot 9H_2O$ ), and citric acid ( $C_6H_8O_7$ ) were separately dissolved in 20 mL of deionized water. Sodium hydroxide (NaOH) was then gradually added dropwise to the solution while stirring continuously at 80°C for 2 hours. Citric acid acted as a chelator agent, absorbing the formation of brown-coloured precipitates. These precipitates were thoroughly washed multiple times with deionized water and acetone to remove impurities. The cleaned precipitates were then dried at 80°C, resulting in dark brown solids. Finally, the dried material underwent calcination at 700°C for three hours in a furnace to obtain the final  $MgFe_2O_4QDs$ .

#### 2.2Characterization techniques

X-ray diffraction (XRD) analysis was conducted to determine the crystalline phase of the MgFe<sub>2</sub>O<sub>4</sub>quantum dots (QDs) using a BRUKER USA D8 Advance, Davinci instrument with CuK $\alpha$  radiation ( $\lambda$  = 1.54060 Å), operating at 40 kV and 30 mA. For morphological characterization, a Scanning Electron Microscope (SEM) was employed using the CARL ZEISS EVO 18 model after sputter-coating the sample. Transmission electron microscopy (TEM) was performed with an FEI TECNAI G2-20 TWIN instrument, operating at 200 kV, to examine the morphology and determine particle size. Selected Area Electron Diffraction (SAED) patterns were recorded by distributing the synthesized sample onto a carbon-coated copper grid.

Elemental composition was analysed using Energy Dispersive X-ray Spectroscopy (EDX) with a Bruker EDX system equipped with an LN<sub>2</sub>-free detector. X-ray photoelectron spectroscopy (XPS) measurements were carried out using the ULVAC-PHI INC model PH150000 version probe 111. The Braeuer-Emmett-Teller (BET) technique was employed to determine the surface area and pore size distribution using the Quanta chrome Instruments Autos-orb IQ series. Fourier transform infrared (FTIR) spectroscopy was performed with a PerkinElmer Spectrum Two instrument. The thermal stability and degradation behaviour of the synthesized sample were evaluated through thermogravimetric and differential thermal analysis (TG/DTA) using a NETZSCH-STA 449 F3 JUPITER instrument. For CV Versa STAT MC model has been used. Finally, cyclic voltammetry (CV) was conducted with a Versa STAT MC model to investigate the electrochemical properties of the sample.

International Journal of Environmental Sciences ISSN: 2229-7359 Vol. 11 No. 18s, 2025 https://theaspd.com/index.php

#### 3. RESULTS AND DISCUSSION

## 3.1 XRD analysis

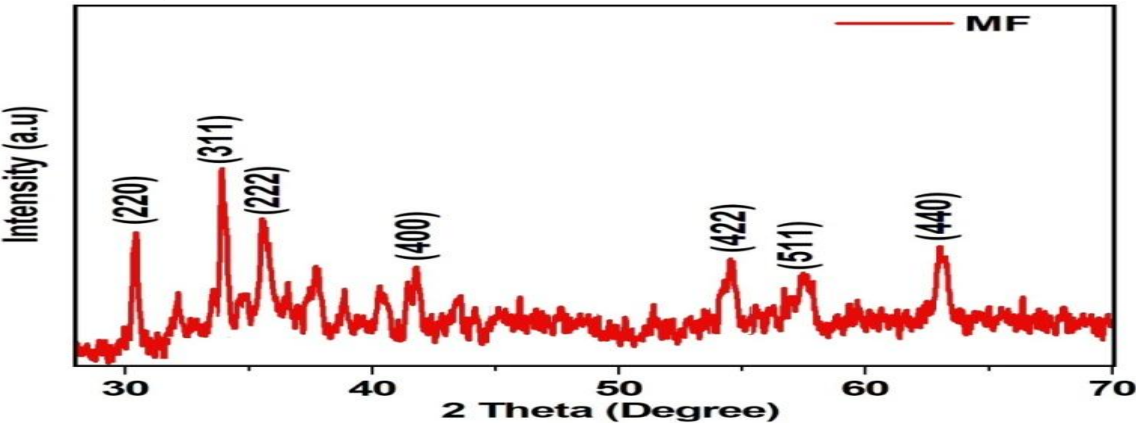


Fig. 1 X-ray diffraction patterns of MgFe<sub>2</sub>O<sub>4</sub> QDs

Fig. 1 gives the XRD patterns of the obtained MgFe<sub>2</sub>O<sub>4</sub> annealed at 700°C for 3 h. The XRD patterns of the MgFe<sub>2</sub>O<sub>4</sub> QDs synthesised through co-precipitation reveal the specific reflections (220), (311), (400), (422), (511) and (440) which are the characteristic of Fd-3m cubic spinel structure [19]. All of the XRD peaks were matched with JCPDS cards 01-1114 (MgFe<sub>2</sub>O<sub>4</sub>). The most intense peak noticed for the (311) plane clearly evidences the formation of the cubic spinel ferrite structure in synthesized sample. The Scherrer's formula [20] used to calculate crystallite size (D) from the (311) peak.

$$D = \frac{0.94 \,\lambda}{\beta_D \cos \theta} \tag{1}$$

Where  $\beta_D$  is the full width at half maximum (FWHM) of diffracting peak,  $\lambda$  is the wavelength of X-ray (0.1541 nm) and  $\theta$  is the Bragg's diffraction angle. The crystallite sizes of the magnesium ferrites were in the range of 12 nm.

#### 3.2 TEM analysis

The TEM image of the synthesized MgFe<sub>2</sub>O<sub>4</sub> quantum dots (QDs), as shown in Fig. 2, confirms that the co-precipitation method produced small spherical nanoparticles. The inset of Fig. 2(a) shows the standard particle size distribution, which was determined to be  $7.62 \pm 0.08$  nm based on TEM analysis. The high-resolution TEM (HRTEM) image in Fig. 2(b) displays the lattice fringes of the crystalline MgFe<sub>2</sub>O<sub>4</sub> nanoparticles, with an estimated d-spacing of approximately 0.25 nm for the (311) plane. This value closely matches the d<sub>311</sub> spacing obtained from the XRD data. Additionally, the selected area electron diffraction (SAED) pattern in Fig. 2(c) exhibits distinct circular rings, characteristic of the cubic spinel structure of MgFe<sub>2</sub>O<sub>4</sub>, with no extra rings observed. The diffraction rings in the SAED pattern align well with the standard reference data (JCPDS: 01-1114) for MgFe<sub>2</sub>O<sub>4</sub> [19].

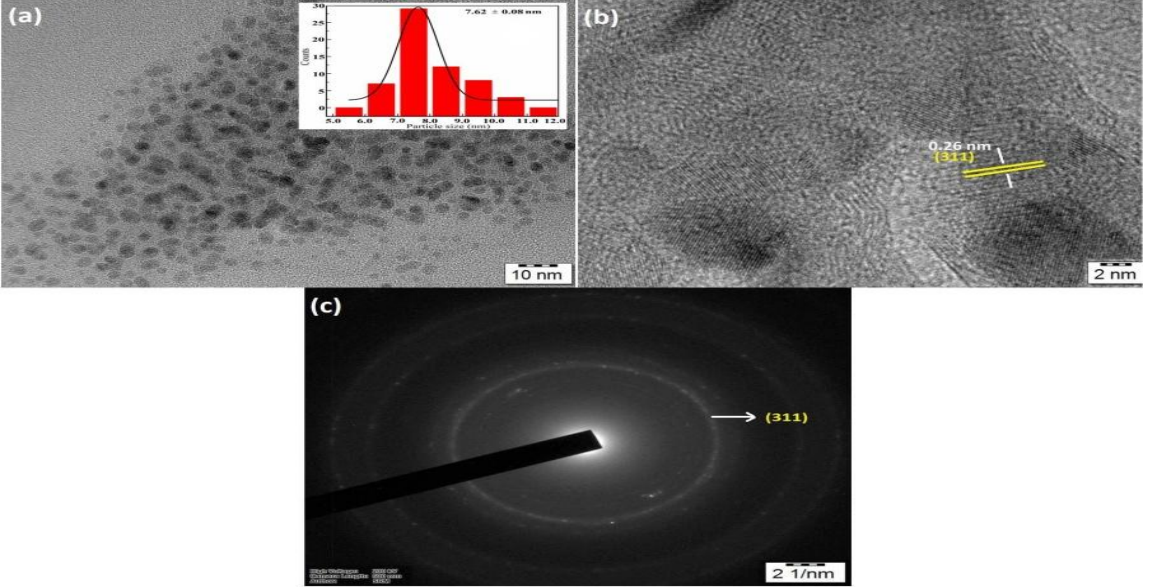


Fig. 2 (a) TEM micrographs (b) HRTEM image and (c) Selected area electron diffraction (SAED) pattern of MgFe<sub>2</sub>O<sub>4</sub> nanoparticles

#### 3.3 SEM and EDX analyses

Fig. 3 (a) and (b) illustrate the elemental mapping of the MgFe<sub>2</sub>O<sub>4</sub> nanoparticles. The SEM micrograph release that the particles exhibit irregular shapes and varying sizes. The elemental mapping confirms the uniform spatial distribution of Mg, Fe, and O throughout the sample. To further validate the even distribution of these elements within the MgFe<sub>2</sub>O<sub>4</sub> nanoparticles, spot EDS study was performed, with the results given in Fig. 3. The EDS spectrum of MgFe<sub>2</sub>O<sub>4</sub> nanoparticles, shown in Fig. 3(c), clearly indicates the presence of Fe, Mg, and O without any noticeable impurities. The atomic peaks similar to iron (Fe), magnesium (Mg), and oxygen (O) are distinctly observed. Additionally, minor peaks were detected, which are likely attributed to contaminants from the sample holder of the instrument.

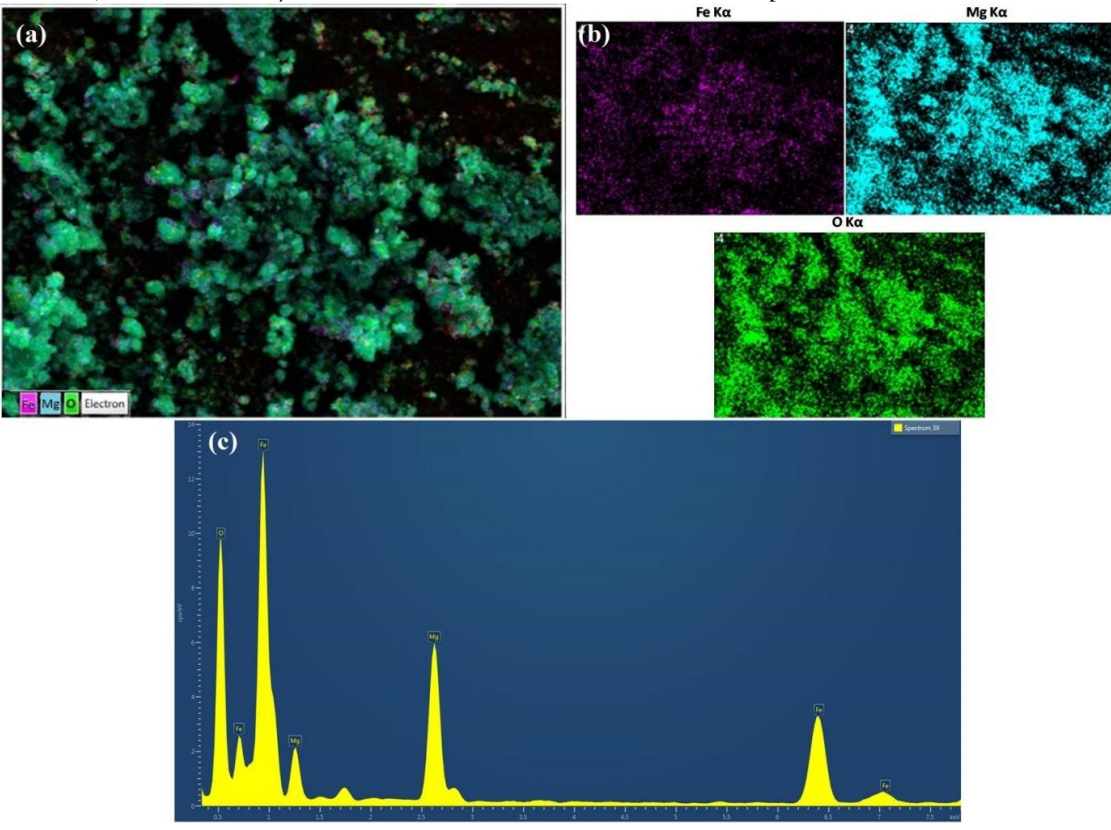


Fig. 3 Scanning electron microscope (SEM) images and energy-dispersive x-ray spectrometer (EDX) elemental maps of the MgFe<sub>2</sub>O<sub>4</sub> nanoparticles

#### 3.4 XPS analysis

X-ray Photoelectron Spectroscopy (XPS) was used to analyze the surface elements, valence states, and binding energies of the  $MgFe_2O_4$  quantum dots (QDs). The XPS results provided a comprehensive spectrum of the  $MgFe_2O_4$  nanoparticles, confirming the existence of Fe, Mg, O, and carbon elements, as shown in Fig. 4.

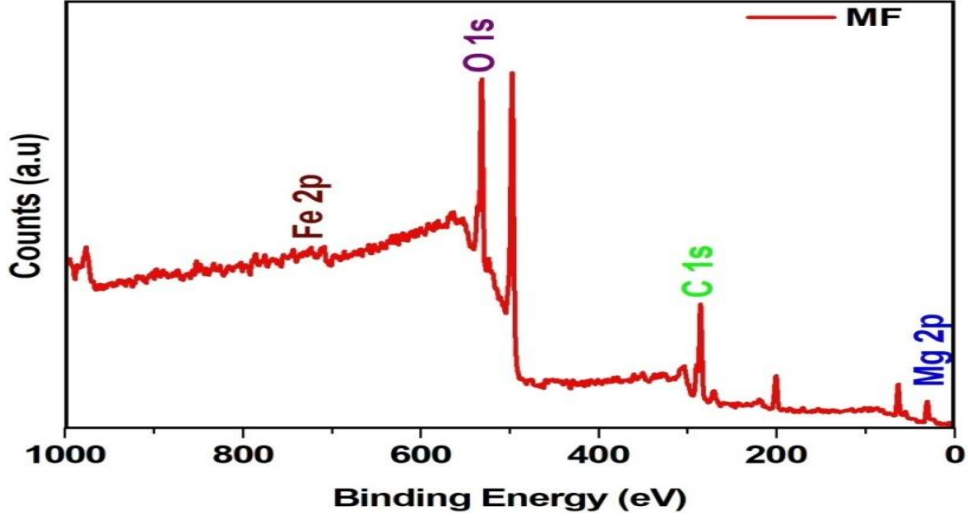


Fig. 4 (a) X-ray photoemission survey spectrum of MgFe<sub>2</sub>O<sub>4</sub> QDs

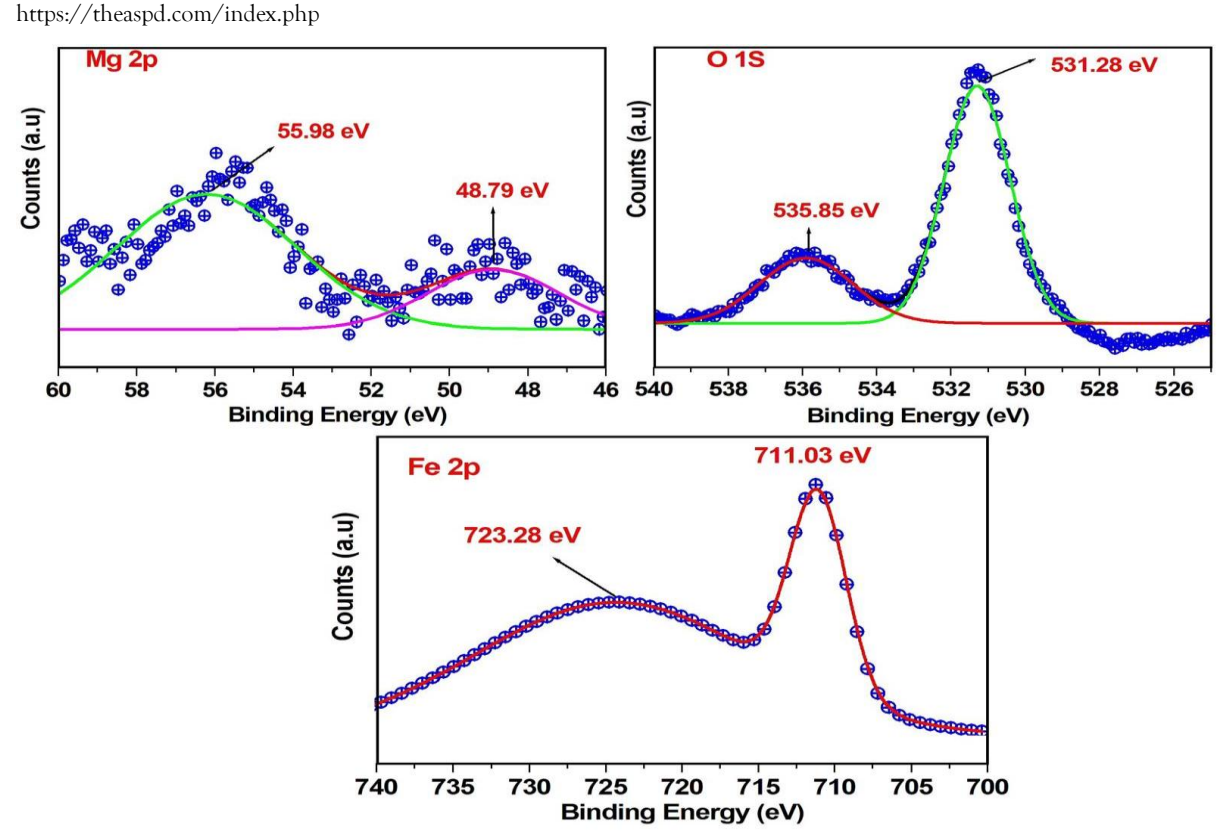


Fig. 5 XPS spectrum of (a) Mg 2p, (b) O 1s and (c) Fe 2p

The C 1s peak observed at 284.37 eV is likely attributed to surface contamination from atmospheric exposure. Further analysis of the individual elemental components was conducted using high-resolution XPS spectra for magnesium (Mg  $2p_3/_2$  and Mg  $2p_1/_2$ ), oxygen (O 1s), and iron (Fe  $2p_1/_2$  and Fe  $2p_3/_2$ ), as illustrated in Fig. 5(a-d). The Mg 2p spectrum, shown in Fig. 5(a), confirms the presence of Mg  $2p_3/_2$  and Mg  $2p_1/_2$  at binding energies of 55.98 eV and 48.79 eV, respectively. The O 1s spectrum, displayed in Fig. 5(d), is deconvoluted into two peaks: the binding energy of 530.85 and 531.28 eV related to 1 s O² ions in the lattices. The high intensity peak at higher energy level of 531.28 eV is corresponding to the perfect energy state of 1 s O² [21]. But the less intensity peak at the lower energy level of 530.85 eV corresponds to the O 1s level in the MgFe<sub>2</sub>O<sub>4</sub> structure [21]. As shown in Fig. 5(c), the Fe 2p spectrum exhibits two distinct peaks at 711.03 eV and 723.28 eV, related to Fe  $2p_3/_2$  and Fe  $2p_1/_2$ , respectively, indicating the presence of iron ions within the MgFe<sub>2</sub>O<sub>4</sub> structure [22]. The XPS results confirm the formation of a spinel structure in the synthesized nanoparticles, with no evidence of secondary phase formation.

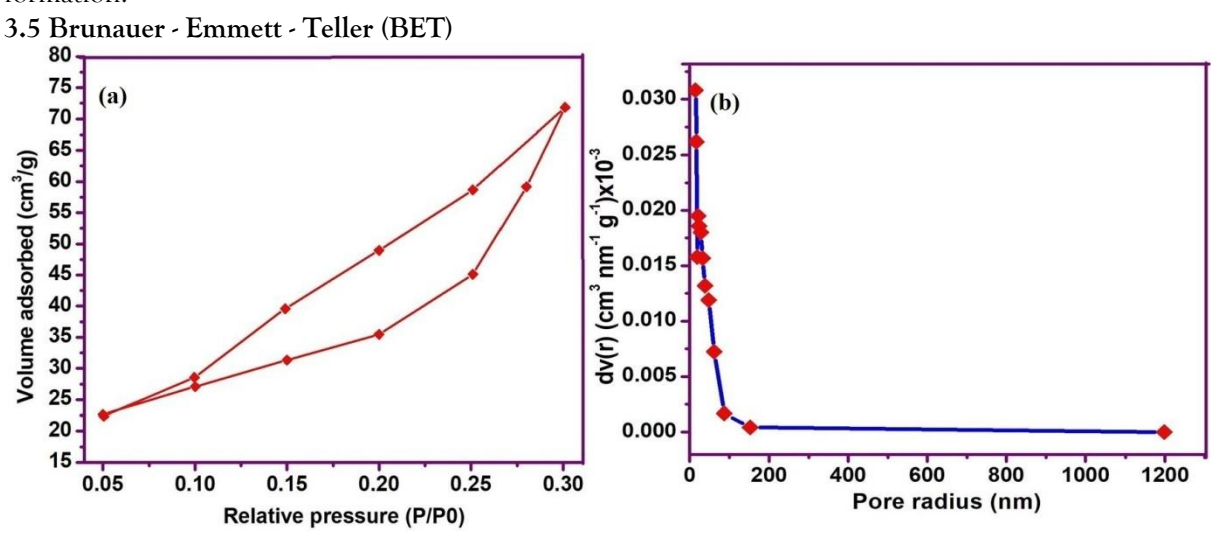


Fig. 6 N<sub>2</sub> adsorption-desorption isotherm of MgFe<sub>2</sub>O<sub>4</sub> nanoparticles.

The nitrogen adsorption-desorption isotherm, which illustrates the adsorption and desorption characteristics of nitrogen gas on the surface of MgFe<sub>2</sub>O<sub>4</sub> quantum dot (QD) nanoparticles, is presented in Fig. 6(a). According to IUPAC classification, the nitrogen adsorption isotherm exhibits a type IV curve

https://theaspd.com/index.php

with an H2 hysteresis loop at relative pressure (P/P<sub>0</sub>) [23,24], as shown in Fig. 6. This observed hysteresis loop suggests the presence of mesoporous MgFe<sub>2</sub>O<sub>4</sub> QDs. The nitrogen adsorption analysis indicates a substantial BET surface area of 39.27 m<sup>2</sup>/g for MgFe<sub>2</sub>O<sub>4</sub>, surpassing previously reported values for MgFe<sub>2</sub>O<sub>4</sub> nanoparticles [23]. Additionally, Fig. 6(b) displays the pore size distribution curve of MgFe<sub>2</sub>O<sub>4</sub> QDs, highlighting the range of pore sizes within the material. The inset of Fig. 6(b) reveals that the predominant pore size in this system is 2.244 nm, with a mesoporous range extending from 18 to 97 nm, signifying a disordered porous structure. The BET results confirm that the highly mesoporous nature of MgFe<sub>2</sub>O<sub>4</sub> offers an abundance of active sites on the surface, which significantly contributes to its super capacitive performance.

## 3.6. FTIR-spectra

Fig. 7 depicts the transmittance FT-IR spectra of the synthesized sample which were annealed at 700 °C for 3 h. FTIR results confirm the spinel structure formation of the MgFe<sub>2</sub>O<sub>4</sub> QDs. The appearance of the band at 1434 cm<sup>-1</sup> was associated with the bending vibration related to the CH<sub>2</sub> groups [19].

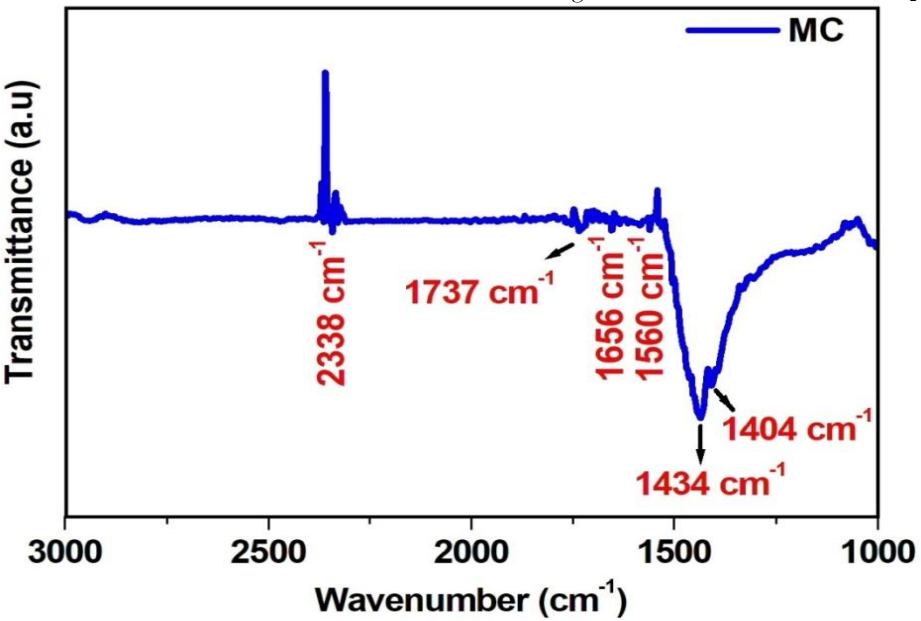
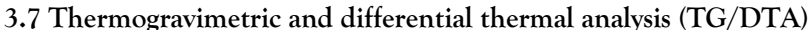


Fig. 7 FTIR spectrum of MgFe<sub>2</sub>O<sub>4</sub> QDs

The bands corresponding to 3000 cm<sup>-1</sup> and 1000 cm<sup>-1</sup> represent stretching and bending vibrations of H–O–H, which indicates the presence of free or absorbed water in the samples. The peak noticed around at 1654 cm<sup>-1</sup> are attributed to the bending vibration of the H–O–H bond in water molecules [25]. The band near at 1562 cm<sup>-1</sup> indicates the C–H bending modes [26]. A high frequency absorption peak was found at 1737 cm<sup>-1</sup>, confirming the presence of O–H groups in the sample [27]. Moreover, the peak at 2327 cm<sup>-1</sup> reveals the O–H stretching vibration of the absorbed water molecule [28].



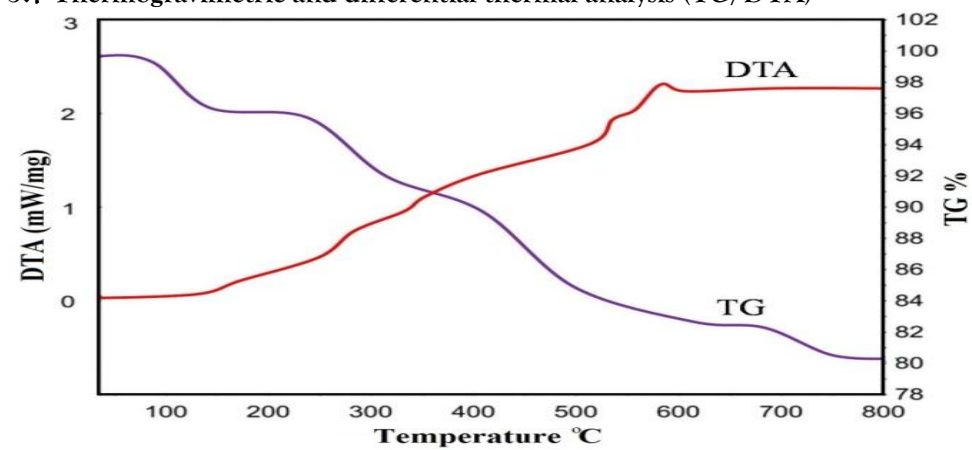


Fig. 8 TG/DTA curve of MgFe<sub>2</sub>O<sub>4</sub>QDs

Thermogravimetric and differential thermal analysis (TG/DTA) was performed on MgFe<sub>2</sub>O<sub>4</sub> quantum dots (QDs) over a temperature range of 30  $^{\circ}$ C to 800  $^{\circ}$ C. The TG/DTA curve, which illustrates the

International Journal of Environmental Sciences ISSN: 2229-7359 Vol. 11 No. 18s, 2025

thermal behaviour of the synthesized sample, is shown in Fig. 8. The first weight loss occurred between 55 °C and 220 °C, primarily due to the evaporation of surface-adsorbed water molecules. The second weight loss, observed between 220 °C and 410 °C, can be credited to the decomposition of organic templates present in the sample [29]. A third weight loss was detected between 410 °C and 650 °C, which is likely associated with a phase transition in the MgFe<sub>2</sub>O<sub>4</sub> QDs. The final weight loss, occurring between 650 °C and 690 °C, indicates the formation of magnesium ferrite. The DTA curve reveals a distinct endothermic peak at approximately 84 °C, corresponding to the dehydration process. Additionally, an exothermic peak at 247 °C suggests the decomposition of nitrates within the sample [30].

#### 3.8 Cyclic Voltammetry

https://theaspd.com/index.php

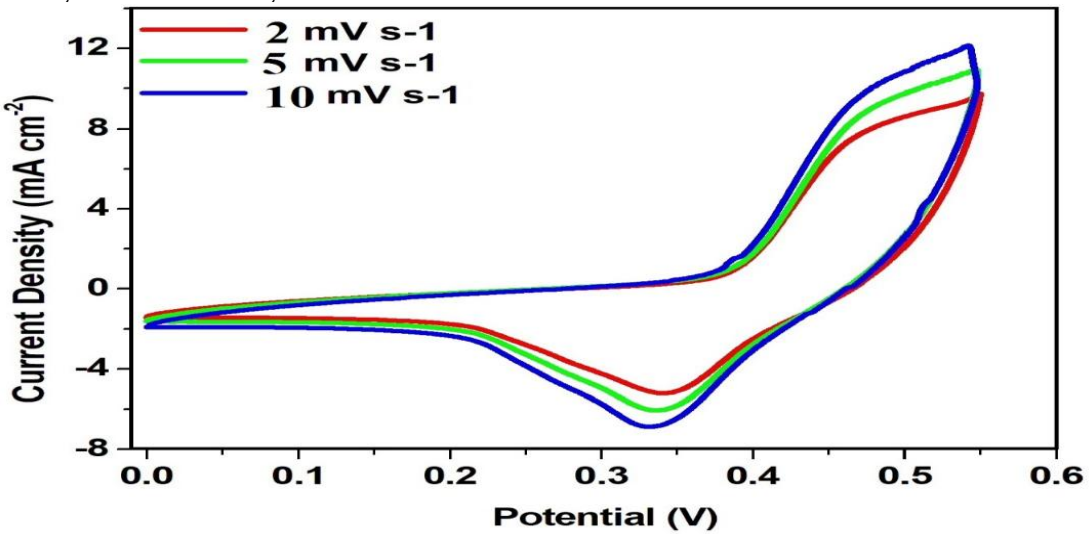


Fig. 9. CV pattern of MgFe<sub>2</sub>O<sub>4</sub> QDs

Electrochemical measurements were conducted using a typical three-electrode configuration consisting of a sample as a working electrode, an Ag/AgCl reference electrode, and a high platinum wire as a counter electrode [31]. In which 0.2 M tetra butyl ammonium perchlorate was taken as electrolyte. From the figure, one can find that sample at 2 mVs<sup>-1</sup> has larger double-layer capacitance in comparison to other scan rates which notices the fast transfer of carriers at the electrode/electrolyte interface [32]. The electrochemical properties of MgFe<sub>2</sub>O<sub>4</sub> QDs were confirmed from cyclic voltammetry (CV). Electrochemical calculation was performed at various scan rates 2, 5, and 10 mV s<sup>-1</sup>as shown in Fig.9. CV patterns are drawn between the current density versus applied potential. At lower scan rates, the CV curves display an ideal rectangular shape, indicative of unmistakable capacitive behaviour [31]. From the CV patterns of the MgFe<sub>2</sub>O<sub>4</sub> sample, which underwent roasting at 700 °C, reveal a pseudo-capacitive nature, as evidenced by changes in the CV curves with increasing scan rate. This indicates the presence of pseudo-capacitive processes within the system, indicating a dynamic capacitive response influenced by the scan rate. Moreover, these oxidation and reduction peaks have shifted to relatively higher and lower applied potentials with an increase in the scan rate [33]. The specific capacitances (Cs) value of the prepared MgFe<sub>2</sub>O<sub>4</sub> electrode was determined by using the following equation [34]

$$Cs = \frac{Q}{A_{VM}} \tag{2}$$

Here,  $C_s$  is the specific capacitance of the electrode material, and Q represents the anodic and cathodic charges that are measured during each cyclic voltammetry (CV) scan. The variable m denotes the mass of the active electrode material (in milligrams), whereas  $\Delta v$  indicates the constant scan rate (mV s<sup>-1</sup>) utilized for the measurements. All CV analyses were conducted within the possible range of 0.0 to 0.6 V.

The almost perfect rectangular shape of the MgFeO<sub>4</sub> CV profile is a sign of capacitive behaviour and is associated with faradaic redox reactions occurring at the surface of the active electrode. The presence of two distinct redox peaks provides more evidence for the electrode material's pseudocapacitive characteristics. As shown in Fig. 9, when the scan rate is increased from low to high values, the oxidation and reduction peak current densities increase correspondingly, and peak positions also migrate slightly. This shift results from rapid and reversible redox reactions occurring on the electrode surface. Interestingly, even at a rather high scan rate of  $10 \text{ mV s}^{-1}$ , the CV curves exhibit good electrochemical reversibility, holding their shape without obvious distortion.

ISSN: 2229-7359 Vol. 11 No. 18s, 2025

https://theaspd.com/index.php

The fact that the specific capacitance was highest at the lowest scan rate was one important discovery. This implies that at slower scan speeds, electrolyte ions have adequate time to permeate into the inner and outer surfaces of the porous electrode construction. However, as ion transport is mainly limited to the outer surface, larger scan speeds result in less efficient usage of the electrode's active regions. Because of MgFe $_2$ O $_4$ 's high mesoporous nature, which appears to increase the active surface area, improved charge storage is made possible.

Thus, the charge storage process involves both faradaic redox contributions and electric double-layer capacitance, with the latter being more significant due to the pseudocapacitive behaviour. Among the recorded scan rates, the electrode at 2 mV s<sup>-1</sup> exhibits the largest capacitive double layer, indicating effective electron-hole separation and charge carrier transport at the electrode-electrolyte interface. The measured specific capacitance values are 260 Fg<sup>-1</sup>, 183 Fg<sup>-1</sup>, and 131 Fg<sup>-1</sup> for scan speeds of 2, 5, and 10 mV s<sup>-1</sup>, respectively. This pattern demonstrates that higher capacitance values can be achieved at lower scan rates, which is highly advantageous for applications involving high-performance supercapacitors.

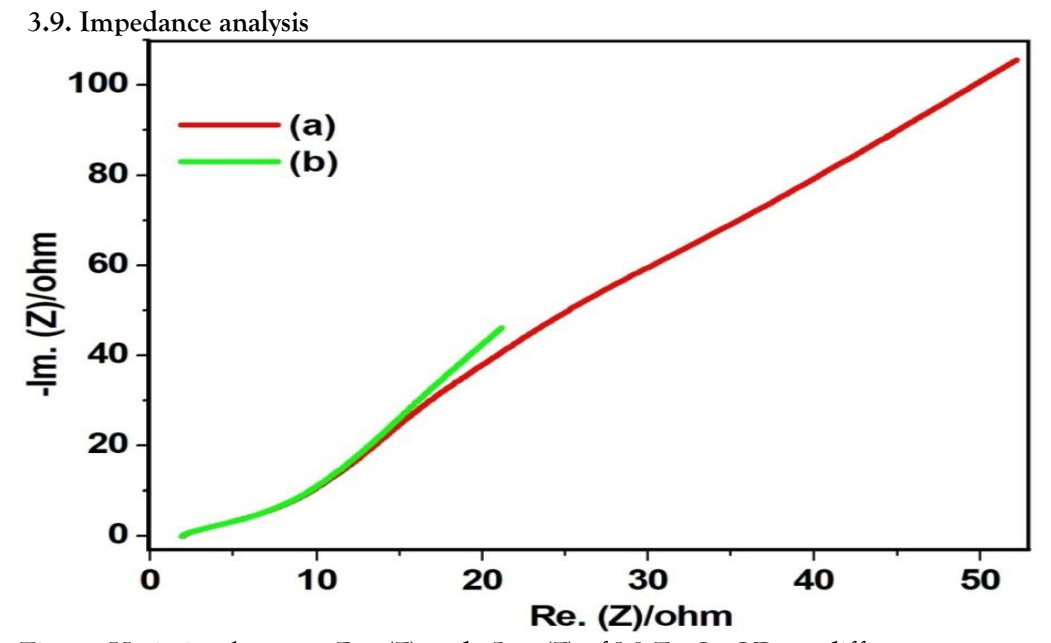


Fig. 10 Variation between Re. (Z) and -Im. (Z) of MgFe<sub>2</sub>O<sub>4</sub> QDs at different temperatures (a) 100 °C and (b) 150 °C

Electrochemical impedance spectroscopy (EIS) was conducted to evaluate the ion transfer pathways and electrical conductivity of MgFe<sub>2</sub>O<sub>4</sub> electrode materials. The Nyquist plots for MgFe<sub>2</sub>O<sub>4</sub> electrodes, displayed in Fig. 10, illustrate both the real and imaginary elements of the impedance spectra. Further analysis of these components provides insights into the presence of grains and grain boundaries, which influence charge transport. Depending on the material structure, conduction can either be long-range (non-localized) or short-range (localized) [35].

The shape of the Nyquist plots (Fig. 9) offers valuable information about different conduction mechanisms and is used to study the relaxation behaviour of the synthesized sample. The presence of multiple semicircles in the Nyquist plot indicates both grain and grain boundary contributions, where the low-frequency semicircle corresponds to grains and the high-frequency semicircle is associated with grain boundaries. Additionally, the intercept of the plot on the real axis shifts as temperature increases, suggesting a limiting material's resistive properties [36]. This shift highlights the bulk resistance (Rb) and grain boundary resistance (Rgb) within the material, emphasizing that the influence of grains is more significant than that of grain boundaries in magnesium ferrites [37, 38].

The impedance analysis confirms that  $MgFe_2O_4$  quantum dots (QDs) exhibit high electrical conductivity and effectively shorten the diffusion distance between the electrolyte and the electrode material, enhancing their electrochemical performance.

#### 4. CONCLUSION

In conclusion, MgFe<sub>2</sub>O<sub>4</sub> quantum dots (QDs) were efficiently synthesized using a cost-effective coprecipitation method. X-ray diffraction (XRD) and Fourier transform infrared spectroscopy (FTIR)

ISSN: 2229-7359 Vol. 11 No. 18s, 2025

https://theaspd.com/index.php

established the formation of a spinel structure in the prepared sample. X-ray photoelectron spectroscopy (XPS) analysis verified the presence of Fe 2p, Mg 2p, and O 1s in the Co-doped MgFe<sub>2</sub>O<sub>4</sub> QDs.

Electrochemical impedance spectroscopy (EIS) results demonstrated that the capacitance performance of MgFe<sub>2</sub>O<sub>4</sub> QD electrodes improved with increasing temperature. Additionally, cyclic voltammetry (CV) analysis indicated that the QDs exhibited the highest specific capacitance at a scan rate of 2 mV/s. These detections suggest that the synthesized MgFe<sub>2</sub>O<sub>4</sub> QDs possess enhanced electrochemical properties, making them a promising material for supercapacitor applications.

#### REFERENCE

- 1. W. Raza, G. Nabi, A. Shahzad, N. Malik and N. Raza, Electrochemical Performance of Lanthanum Cerium Ferrite Nanoparticles for Supercapacitor Applications, J Mater Sci: Mater Electron., 32 (2021) 7443–7454.
- 2. G. Nabi, K. N. Riaz, M. Nazir, W. Raza, M. B. Tahir, M. Rafique, N. Malik, A. Siddiqa, S. S. Ali Gillani, M. Rizwan, M. Shakil and M. Tanveer, Cogent synergic effect of TiS2/g-C3N4 composite with enhanced electrochemical performance for supercapacitor. Ceramics International, 46 (2020) 27601-27607.
- 3. W. Zhang, B. Quan, C. Lee, S. K. Park, X. Li, E. Choi, G. Diao and Y. Piao, One-Step Facile Solvothermal Synthesis of Copper Ferrite—Graphene Composite as a High-Performance Supercapacitor Material, ACS Appl. Mater. Interfaces, 7 (2015) 2404–2414.
- 4. S. Thankachan, S. Xavier, B. Jacob, and E. M. Mohammed, A comparative study of structural, electrical and magnetic properties of magnesium ferrite nanoparticles synthesised by sol-gel and co-precipitation techniques, J. Experimental Nanoscience, 8 (2013) 347–357.
- 5. E. Veena Gopalan, I.A. Al-Omari, K.A. Malini, P.A. Joy, D. Sakthi Kumar, Y. Yoshida, and M.R. Anantharaman, Impact of zinc substitution on the structural and magnetic properties of chemically derived nanosized manganese zinc mixed ferrites, J. Magn. Magn. Mater. 321 (2009) 1092–1099.
- 6. M. Srivastava, S. Chaubey, and A.K. Ojha, Investigation on size dependent structural and magnetic behavior of nickel ferrite nanoparticles prepared by sol-gel and hydrothermal methods, Mater. Chem. Phys. 118(1) (2009) 174–180.
- 7. Y. L. Liu, Z. M. Liu, Y. Yang, H. F. Yang, G. L. Shen, and R. Q. Yu, Simple synthesis of MgFe2O4 nanoparticles as gas sensing materials, Sens. Actuators B, 107 (2005) 600–604.
- 8. Z. H. Hua, R. S. Chen, C. L. Li, S. G. Yang, M. Lu, X. B. Gu and Y. W. Du, CoFe<sub>2</sub>O<sub>4</sub> nanowire arrays prepared by template-electrodeposition method and further oxidization, J. Alloys Compd., 427, (2007) 199-210.
- 9. A. Tufani, A. Qureshi and J. H. Niazi, Iron oxide nanoparticles based magnetic luminescent quantum dots (MQDs) synthesis and biomedical/biological applications: A review, Mater. Sci. Eng. C, 118 (2021) 111545-111566.
- 10. K. B. Riad, S. V. Hoa and P. M. W. Adam, Metal Oxide Quantum Dots Embedded in Silica Matrices Made by Flame Spray Pyrolysis, ACS Omega, 6 (2021) 11411–11417.
- 11. A. Baldelli, H. Etayash, H. Oguzlu, R. Mandal, F. Jiang, R. E. W. Hancock and A. P. Singh, Antimicrobial properties of spray-dried cellulose nanocrystals and metal oxide-based nanoparticles-in-microspheres, Chem. Eng. J. Adv., 10 (2022) 100273-100287.
- 12. A. P. Litvin, I. V. Martynenko, F. P. Milton, A. V. Baranov, A. V. Fedorov and Y. K. Gunko, Colloidal quantum dots for optoelectronics, J. Mater. Chem. A,5 (2017) 13252-13275.
- 13. Y. L. Liu, Z. M. Liu, Y. Yang, H. F. Yang, G. L. Shen, and R. Q. Yu, Simple synthesis of MgFe2O4 nanoparticles as gas sensing materials, Sens. Actuators B, 107 (2005) 600–604.
- 14. U.S. Sharma, R.N. Sharma, R. Shah, Physical and magnetic properties of manganese ferrite nanoparticles, Int. J. Eng. Res. Afr., 4 (8) (2014) 14–17.
- 15. M. W. Mushtaq, M. Shahbaz, R. Naeem, S. Bashir, S. Sharif, K. Alia and N. A. Dogar, Synthesis of surfactant-assisted nickel ferrite nanoparticles (NFNPs@surfactant) to amplify their application as an advanced electrode material for high-performance supercapacitors, RSC Adv., 14 (2024) 20230-20240.
- 16. A. Raza, K. Sayeed, A. Naaz, M. Muaz, S. N. Islam, S. Rahaman, F. Sama, K. Pandey and A. Ahmad, Green Synthesis of ZnO Nanoparticles and Ag-Doped ZnO Nanocomposite Utilizing Sansevieria trifasciata for HighPerformance Asymmetric Supercapacitors, ACS Omega, 9 (2024) 32444—32454.
- 17. K. Seevakan, A. Manikandan, P. Devendran, Y. Slimani, A. Baykal and T. Alagesan, Structural, magnetic and electrochemical characterizations of Bi2Mo2O9 nanoparticle for supercapacitor application, J. Magn. Magn Mater., 486 (2019), 165254-165262. 18. M. Murugesan, N. Nallamuthu, R. Ranjithkumar, M. Krishnakumar, P. Devendran and K. Ramesh, Synthesis and electrochemical investigation of hetero bimetallic complexes CoMn2O4 micro rods for novel supercapacitor electrode, Electron. Mater. Lett., 19 (1) (2023) 108–118.
- 19. M. G. Naseri, M. H. M. Ara, E. B. Saion and A. H. Shaar, Super-paramagnetic magnesium ferrite nanoparticles fabricated by a simple, thermal-treatment method, J. Magnetism and Magnetic Materials, 350 (2014) 141–147.
- 20. B.D. Cullity, Elements of X-ray Diffraction, Addison-Wesley, London, 1959.
- 21. S. S. Guzman, B. R. Jayan, E. d. Rosa, A. T. Castro, V. G. Gonzalez and M. J. Yacaman, Synthesis of assembled ZnO structures by precipitation method in aqueous media, Mater.Chem. Phys., 115 (2009) 172-178.
- 22. M. Silva, V. Murzin, L. Zhang, J. Baltrus and J. Baltrusaitis, Transition Metal Doped MgO Nanoparticles for Nutrient Recycling: An Alternate Mg Source for Struvite Synthesis from Wastewater, Environmental Science: Nano, 7 (2020)3482–3496. 23. A. Monunith, A. Rajan and N. K. Sahu, Comparative study of enzymatic and non-enzymatic detection of glucose using
- manganese ferrite nanoparticles, Mater. Res. Express, 7 (9) (2020).

  24. C. O. Ania, A. Gomis-Berenguer, J. Dentzer and C. Vix-Guterl, Nanoconfinement of glucose oxidase on mesoporous carbon electrodes with tunable pore sizes, J. Electroanal. Chem., 808 (2018) 372–379.
- 25. L. A. Kafshgari, M. Ghorbani and A. Azizi, Synthesis and characterization of manganese ferrite nanostructure by coprecipitation, sol-gel, and hydrothermal methods, Particulate Sci. Technol., 37 (2018) 904–910.

ISSN: 2229-7359 Vol. 11 No. 18s, 2025

https://theaspd.com/index.php

- 26. R. Sundari, T. I. Hua, M. Aziz and D. Nizar, The characterization study of ferrites (magnesium and manganese) using sol gel method, The Malaysian J. Analytical Sciences, 18 (2014) 485–490.
- 27. M. M. N. Ansari, S. Khan and N. Ahmad, Effect of R3+ (R= Pr, Nd, Eu and Gd) substitution on the structural, electrical, magnetic and optical properties of Mn-ferrite nanoparticles, J. Magn. Magn. Magn. Magn. 81-87.
- 28. A. M. Jacintha, V. Umapathy, P. Neeraja and S. R. J. Rajkumar, Synthesis and comparative studies of MnFe2O4 nanoparticles with different natural polymers by sol-gel method: structural, morphological, optical, magnetic, catalytic and biological activities, J. Nanostruct. Chem., 7 (2017) 375–387.
- 29. D. Raouf, Synthesis and microstructural properties of ZnO nanoparticles prepared by precipitation method, Renewable Energy, 50 (2013) 932-937.
- 30. P. Sivagurunathan and S. R. Gibin, Preparation and characterization of nanosized cobalt ferrite particles by co-precipitation method with citrate as chelating agent, J. Mater. Sci. Mater. Electron. 27 (2016) 8891–8898.
- 31. K. Sathishkumar, N. Shanmugam, N. Kannadasan, S. Cholan and G. Viruthagiri, Opto, magnetic and electrochemical characterization of Ni1–xCoxO nanocrystals, J. Mater. Sci. Mater. Electron. 26 (2015) 1881–1889.
- 32. D. Abisha, S. R. Gibin, V. K. PremKumar and A. Mariappan, Improved supercapacitor application of manganese ferrite nanoparticles via co-precipitation technique, Heliyon, 9 (2023) 21120-21131.
- 33. S. C. Pang, B. H. Wee and S. F. Chin, The capacitive behaviors of manganese dioxide thin-film electrochemical capacitor prototypes, Int. J. Electrochem., 2011 (2011).
- 34. N. Kitchamsetti, Y. R. Ma, P. M. Shirage and R. S. Devan, Mesoporous perovskite of interlocked nickel titanate nanoparticles for efficient electrochemical supercapacitor electrode, Journal of Alloys and Compounds, 833 (2020) 155134-155147.
- 35. A. K. Behera, N. K. Mohanty, S. K. Satpathy, B. Behera and P. Nayak, Investigation of complex impedance and modulus properties of Nd doped 0:5BiFeO<sub>3</sub>-0:5PbTiO<sub>3</sub> multiferroic composites, Cent. Eur. J. Phys., 12 (2014) 851-861.
- 36. M. Kashif, M. E. Ali, S. M. U. Ali, U. Hashim and S. B. Abd Hamid, Impact of hydrogen concentrations on the impedance spectroscopic behavior of Pd-sensitized ZnO nanorods, Nanoscale Res. Lett., 8 (2013) 1–9.
- 37. S. K. Barik, R. N. P. Choudhary, P. K. Mahapatra, Impedance spectroscopy study of  $Na1/2Sm1/2TiO_3$  ceramic, Appl. Phys. Mater. Sci. Process, 88 (2007) 217–222,
- 38. S. R. Gibin, P. Sivagurunathan, Synthesis and characterization of nickel cobalt ferrite (Ni<sub>1-x</sub>Co<sub>x</sub> Fe<sub>2</sub>O<sub>4</sub>) nano particles by coprecipitation method with citrate as chelating agent, J. Mater. Sci. Mater. Electron. 28 (2017) 1985–1996.